ARTICLE IN PRESS

Engineering xxx (xxxx) xxx

Contents lists available at ScienceDirect

Engineering

journal homepage: www.elsevier.com/locate/eng

Article

Cu Distribution Pattern Controlled Active Species Generation and Sulfamethoxazole Degradation Routes in a Peroxymonosulfate System

Ning Li [a], Haoxi Dai [a], Mengting He [a], Jun Wang [b], Zhanjun Cheng [a,*], Beibei Yan [a], Wenchao Peng [b,*], Guanyi Chen [c,d,*]

[a] School of Environmental Science and Engineering/Tianjin Engineering Research Center of Bio Gas/Oil Technology, Tianjin University, Tianjin 300072, China
[b] Department of Chemical Engineering, Tianjin University, Tianjin 300350, China
[c] School of Mechanical Engineering, Tianjin University of Commerce, Tianjin 300134, China
[d] School of Science, Tibet University, Lhasa 850012, China

ARTICLE INFO

Article history:
Available online xxxx

Keywords:
Cu cluster
Distribution pattern
Peroxymonosulfate
Active species
Degradation routes

ABSTRACT

The distribution pattern of metals as active centers on a substrate can influence the peroxymonosulfate (PMS) activation and contaminants degradation. Herein, atomic layer deposition is applied to prepare Cu single atom (SA-Cu), cluster (C-Cu), and film (F-Cu) decorated MXene catalysts by regulating the number of deposition cycles. In comparison with SA-Cu-MXene (adsorption energy (E_{ads}) = −4.236 eV) and F-Cu-MXene (E_{ads} = −3.548 eV), PMS is shown to adsorb preferably on the C-Cu-MXene surface for activation (E_{ads} = −5.435 eV), realizing higher utilization efficiency. More $SO_4^{\bar{\cdot}}$ are generated in C-Cu-MXene/PMS system with steady-state concentration and 1–3 orders of magnitude higher than those in the SA-Cu-MXene and F-Cu-MXene activated PMS systems. Particularly, the contribution of $SO_4^{\bar{\cdot}}$ oxidation to sulfamethoxazole (SMX) degradation followed the order, C-Cu-MXene (97.3%) > SA-Cu-MXene (90.4%) > F-Cu-MXene (71.9%), realizing the larger SMX degradation rate in the C-Cu-MXene/PMS system with the degradation rate constants (k) at 0.0485 min^{-1}. Additionally, SMX degradation routes in C-Cu-MXene/PMS system are found with fewer toxic intermediates. Through this work, we highlighted the importance of guided design of heterogeneous catalysts in the PMS system. Appropriate metal distribution patterns need to be selected according to the actual water treatment demand. Metal sites could be then fully utilized to produce specific active species to improve the utilization efficiency of the oxidants.

© 2023 THE AUTHORS. Published by Elsevier LTD on behalf of Chinese Academy of Engineering and Higher Education Press Limited Company. This is an open access article under the CC BY-NC-ND license (http://creativecommons.org/licenses/by-nc-nd/4.0/).

1. Introduction

Recently, peroxymonosulfate (PMS)-based Fenton-like reaction has received increasing attention for wastewater treatment [1]. The active species with high oxidation activity such as hydroxyl radicals (·OH), sulfate radicals ($SO_4^{\bar{\cdot}}$), and singlet oxygen ($^1O_2$) can be generated in a PMS system for organic contaminants degradation [2–4]. The homogeneous Fenton-like reactions with high metal atom utilization (~100%) have been extensively employed in water treatment [5]. Nonetheless, the homogeneous catalysts cannot be recycled, bringing secondary pollution, which requires further safe disposal [6].

The heterogeneous system integrates the merits of more tolerance towards strong acid or base conditions and well-recyclability compared with the homogeneous one, which has aroused increasing attention [7]. Currently, heterogeneous catalysts such as metal oxides and metal-loaded carbon materials (e.g., activated carbon, carbon nanotube, biochar, and graphene oxide) have been investigated intensively [8–11]. The above catalysts play an overwhelming role in Fenton-like oxidation processes. Nevertheless, heterogeneous catalysis usually occurs on a catalyst surface with low atomic utilization efficiency. Only a small fraction of the metals exhibited catalytic activity, owing to the inevitable aggregation of hundreds or thousands of metal atoms in the catalyst. Moreover, metal leakage may occur when excessive metals and metal oxides are used in the Fenton-like reactions. Consequently, more efficient and stable catalysts are needed to be developed urgently, in order to be able to achieve rapid release and effective utilization of active species.

Single-atom catalysts with high atom utilization efficiency, as well as complete exposure of the active sites and high catalytic activity, are desirable in heterogeneous systems [12–14]. However,

* Corresponding authors.
E-mail addresses: zjcheng@tju.edu.cn (Z. Cheng), wenchao.peng@tju.edu.cn (W. Peng), chen@tju.edu.cn (G. Chen).

https://doi.org/10.1016/j.eng.2023.07.020
2095-8099/© 2023 THE AUTHORS. Published by Elsevier LTD on behalf of Chinese Academy of Engineering and Higher Education Press Limited Company.
This is an open access article under the CC BY-NC-ND license (http://creativecommons.org/licenses/by-nc-nd/4.0/).

Please cite this article as: N. Li, H. Dai, M. He et al., Cu Distribution Pattern Controlled Active Species Generation and Sulfamethoxazole Degradation Routes in a Peroxymonosulfate System, Engineering, https://doi.org/10.1016/j.eng.2023.07.020

a sharp increase in the free energy was observed on the metal surface due to the increase of the specific surface area, such as when metal particles were reduced to a single-atom level [15]. Also, migration and agglomeration of the atoms during preparation and reaction processes can result in catalyst deactivation. Subnanometallic clusters with size between single atoms and nanoparticles (NPs) exhibited ring, close-packed, or cage-like structures with stronger interactions between atoms [16]. Clusters with higher stability provided continuous active sites for catalytic reactions compared with Single-atom catalysts. In addition, clusters with high surface-to-volume ratios allowed for higher metal utilization than larger-size NPs. Also, the metal–metal bonds and defined low-core metal active centers in clusters showed unique catalytic performance. For the first time, Peng et al. [17] prepared *Enteromorpha*-derived iron–nitrogen–carbon (Fe-N-C) catalysts by pyrolysis and observed Fe clusters and atomically dispersed Fe-N_x sites. The Fe-N-C/PMS system exhibited high activity in degrading organic pollutants. Noticeably, the metal distribution modes (single atoms, clusters, and NPs) have influenced the active sites of catalysts, which in turn affected the active species production and oxidation selectivity during pollutants degradation. However, the effect of metal distribution modes on PMS activity is still lacking in literature, especially, with respect to contaminants degradation role by metal distribution-based persulfate [18]. The activation mechanism of different metal distribution modes such as adsorption energy and charge transfer in the PMS system remained unclear.

Cu-based catalysts, with diverse activation pathways, are regarded as one of the most effective catalysts to activate PMS (Table S1 in Appendix A) [13]. Furthermore, MXene with unique two-dimensional (2D) layered nanostructure and sheet surface electronegativity, promotes the uniform distribution of metals [12]. Atomic layer deposition (ALD) possesses the advantages of uniform deposition and controlled process, which were exploited in this study to gain atomic-level control of catalyst composition and structure [19]. Sulfamethoxazole (SMX) is one of the common antibiotics among the top three used sulfonamides, which poses a serious threat to humans and the ecological environment [12,20]. Therefore, SMX was selected as the target pollutant in this work [20,21]. The single atom (SA), cluster (C), and film (F) of Cu were deposited on the surface of MXene (denoted as SA-Cu-MXene, C-Cu-MXene, and F-Cu-MXene, respectively) by ALD for SMX degradation in a Fenton-like system. The objectives of this study are as follows: ①Prepare Cu-decorated MXene samples in a controlled manner with emphasis on the characterization of Cu single atoms and clusters; ②investigate the performance of three Cu-decorated MXene samples for PMS activation; ③study the generation and contribution rule of active species in Cu-MXene/PMS systems; ④discuss the adsorption energy and charge transfer of C-Cu-MXene in the process of PMS activation by the density functional theory (DFT); and finally ⑤explore the pathways and toxicity changes during SMX degradation in different Cu-decorated MXene/PMS systems. The work is aimed to provide a precise strategy for Cu-decorated MXene preparation. Accordingly, the influence rule of Cu distribution pattern on PMS activation was systematically elucidated, which can offer theoretical guidance to utilize metal sites efficiently and regulate the oxidation process based on the goal orientation in a PMS-based advanced oxidation system.

2. Materials and methods

2.1. Chemicals

All chemicals were utilized directly in the experiments without further purification. The deionized water was served as solvent. The Ti_3C_2-based MXene nanosheets was fabricated by etching the Al layers of Ti_3AlC_2 ceramic in HCl/LiF solution [1]. The diethyl zinc (Et_2Zn, > 99.9%) and dimethylamino-2-propoxide ($Cu(damp)_2$, > 99.9%) precursors were ordered from Nanjing Aimouyuan Scientific Equipment Co. Ltd. Sulfamethoxazole as the target contaminant and acetic acid were provided by Nine Ding Chemistry Company (Shanghai, China). Tert-butyl alcohol sodium carbonate (Na_2CO_3), L-histidine, methanol, furfuryl alcohol (FFA), nitrobenzene (NB), 5,5-dimethyl-1-pyrroline-*N*-oxide (DMPO) and 2,2,6,6-tetramethyl-4-piperidone (TEMP) were supplied by Shanghai Aladdin Biochemical Technology Co., Ltd. (China). Benzoic acid (BA) was provided by Alfa Aesar company (the United Kingdom). Potassium monoperoxysulfate (PMS; $2KHSO_5{\cdot}KHSO_4{\cdot}K_2SO_4$), sodium acetate, borax and boric acid were obtained from Tianjin Heowns Biochemical Technology Co., Ltd. (China). Sodium thiosulfate pentahydrate was offered by Tianjin North Tianyi Co., Ltd. (China). Chloroform was acquired from Tianjin Real&Lead Chemical Co., Ltd. (China). High purity nitrogen (N_2, 99.999%) was available from Haolun Gas Company (Tianjin, China).

2.2. Synthesis of Cu-decorated MXene catalysts

The Cu-decorated MXene samples were synthesized using an ALD reactor (MNT-S100-L3S1; Jiangsu MNT Micro and Nanotech Co., Ltd, China). Specifically, 0.1500 g Ti_3C_2-based MXene was added to the ALD chamber. The deposition was performed at 120 °C. During this process, high-purity N_2 was introduced into the ALD chamber as a carrier gas at a flow rate of 50 standard cubic centimeter per minute (sccm). Cu was obtained by the self-limiting reactions between Et_2Zn and $Cu(damp)_2$. $Cu(damp)_2$ and Et_2Zn were maintained at 100 and 25 °C using the heated hood, respectively. Both precursors were pulsed into the ALD chamber alternately and chemisorbed onto the MXene powder. The residual precursors and by-products were purged out sufficiently by N_2. Importantly, 50–200 consecutive pulses of $Cu(damp)_2$ followed by 50–200 consecutive pulses of Et_2Zn were applied to ensure adequate adsorption in one deposition cycle. Clearly, one ALD cycle employed in this study consisted of a 2 s pulse, 5 s exposure, and 20 s purge of $Cu(damp)_2$, then 0.5 s pulse, 5 s exposure, and 20 s purge of Et_2Zn. After 1, 3, and 150 deposition cycles, the Cu-decorated MXene catalysts were successfully fabricated.

2.3. Characterization of Cu-decorated MXene catalysts

The morphology of the catalysts was observed using a scanning electron microscope (SEM; Genimi 500; Zeiss, Germany) and a transmission electron microscope (TEM; JEM-2100F, JEOL, Japan). The crystal structure and plane spacing of the catalysts were obtained by high resolution transmission electron microscope (HRTEM; JEM-2100F, JEOL, Japan). The elemental distribution in the catalysts was observed by an X-ray energy dispersive spectrometer (EDS; Ultim Extreme, United Kingdom) and an aberration-corrected high-angle annular dark-field scanning transmission electron microscopy (AC-HAADF-STEM; Titan Cubed Themis G2300, Netherlands). The crystalline phase of the catalyst was determined by an X-ray diffractometer (XRD; Smart Lab; Rigku, Japan). The surface functional groups were determined via Fourier transform infrared spectrometer (FTIR; Nicolet iN10, Thermo Fisher Scientific, USA). The surface elemental composition was analyzed by X-ray photoelectron spectroscopy (XPS; Thermo Scientific K-Alpha+, Thermo Fisher Scientific, USA) with a monochromatic Al-Kα source (1486.6 eV) for excitation. Raman spectra were collected with a micro Raman imaging spectrometer (DXR3xi; Thermo Fisher Scientific, USA). The N_2 adsorption–desorption characteristics of the samples were determined by a surface area analyzer (Autosorb-1-C; Quantachrome Instrument,

USA) at −196 °C. The reactive oxygen species (ROS) in the system were verified by an electron paramagnetic resonance (EPR; Bruker E 500, BioSpin, Germany). X-ray absorption fine structure (XAFS) spectra were collected at the Beijing Synchrotron Radiation Facility (BSRF, China) in transmission mode on the 1W1B beamline. The Cu K-edge extended X-Ray absorption fine structure (EXAFS) spectroscopy was recorded in transmission mode. Two scans were performed on a particular sample, and the linearity and peak position of the Cu K-edge X-ray absorption near-edge structure (XANES) spectrum did not change significantly. The XAFS spectra of standard samples (Cu_2O, CuO, and Cu foil) were recorded in transmission mode. The atlas was processed and analyzed by the software code Athena and Artemis (USA). The mineralization rate of wastewater was determined by the total organic carbon analyzer (TOC; TOC-L, Shimadzu, Japan). The degradation intermediates and potential degradation routes of SMX were analyzed via liquid chromatography–mass spectrometry (LC–MS; LC-20AD, Shimadzu, Japan).

2.4. Batch experiments and analytical methods

The catalyst activity was evaluated in a beaker (150 mL) with continuous stirring at temperature (T) at 25 °C. Typically, the catalyst powder (0.5 g·L^{-1}) was added to SMX (15 mg·L^{-1}) borax buffer solution (pH = 7). The solution pH was kept stable throughout the reactions. Subsequently, a certain amount of PMS was added to the system. At specific time intervals, 0.9 mL of the solution was collected from the mixture using a syringe and filtered through a 0.22 μm membrane. Immediately, it was added to a glass vial containing 0.1 mL of $Na_2S_2O_3$ (0.5 mol·L^{-1}) to ensure the suspension of reactions. The probes, including 10 mmol·L^{-1} FFA, 10 mmol·L^{-1} NB, and 10 mmol·L^{-1} BA were applied to determine the ROS in Cu-decorated MXene/PMS systems. The SMX concentration was measured by high-performance liquid chromatography (HPLC; Agress 1100, China) equipped with a C18 column (4.6 mm × 150 mm × 5 μm) and ultraviolet (UV) detector at 264 nm [22]. The PMS utilization was measured by iodine titration.

2.5. DFT calculation process

The DFT calculations were performed by the Vienna Ab initio Simulation Package [23–27]. The Perdew–Burke–Ernzerhof exchange–correlation function and projector-augmented wave scheme were applied to describe ion–electron exchange–correlation [27,28]. The energy cutoff for the plane wave basis set was 450 eV. The DFT-D3 method was utilized to consider the correction of the van der Waals interaction [29]. The Brillouin zone was sampled with a gamma-centered grid of 2 × 2 × 1 throughout the computational process [30]. During geometry optimization, the force on each atom was set to 0.02 eV/Å. A vacuum region of 20 Å along the vertical direction was added to avoid the interaction in the adjacent periodic images. The adsorption energy of PMS was calculated according to Eq. (1),

$$E_{ads} = E_{total} - E_{sub} - E_{PMS} \quad (1)$$

where E_{total} is the total energy of the PMS adsorbed on the substrate, E_{sub} and E_{PMS} are the energies of the clean substrate and PMS molecule, respectively.

3. Results and discussion

3.1. Characteristics of Cu-decorated MXene

According to SEM, TEM, and HRTEM images, the copper oxide was deposited successfully on the MXene surface (Fig. S1 in Appendix A). The (002) and (−111) planes of CuO were recognized through the XRD pattern (Fig. S2 in Appendix A). Moreover, the surface functional groups (e.g., O—H and C=O) in Cu-decorated MXene samples could be observed by FTIR spectra (Fig. S2). Also, the SA-Cu-MXene and C-Cu-MXene showed the presence of more defects than F-Cu-MXene (Fig. S2). EDS mapping confirmed that Cu film was distributed uniformly on the MXene substrate (Fig. S3 in Appendix A). No manifested interaction between Cu and C atoms can be found (Figs. S4–S6 in Appendix A). The total Cu content rose from 0.15 at% to 1.3 at% with the ALD cycles from 1 to 150. (Fig. S6(d)). From combined HRTEM and XRD analysis, it could be speculated that partial Cu atoms might be anchored on the MXene surface via metal–oxygen bonds. However, the accurate coordination environment of Cu should be further confirmed by XAFS analysis.

The difference between Cu single-atoms and clusters on the MXene surface could be identified by AC-HAADF-STEM observation. As shown in Figs. 1(a) and (b), the bright spots with a single-atom size were distributed on the surface of SA-Cu-MXene. Visibly, Cu atoms were successfully loaded. Under suitable pulse frequency and ALD cycle, the Cu atom agglomeration could be kept to a minimum and mainly remained in the form of micro-clusters. As depicted in Figs. 1(c) and (d), Cu clusters (yellow circles) were noticed on the MXene surface after three cycles of deposition. However, improper sampling might lead to "defective pixels" in the scanning process, resulting in misjudgment of Cu atoms.

XANES and extended EXAFS were applied to further characterize the atomic dispersion and coordination environments of the catalysts. The XANES was performed at the Cu K-edge, with Cu_2O, CuO, and Cu foil as the references. As shown in Fig. 2(a), the sample absorption edge was close to the one of Cu_2O and Cu standards. Obviously, the Cu valence state in C-Cu-MXene was likely to be higher than that of metallic Cu^0 but lower than that of Cu^{1+}. As illustrated in Fig. 2(b), the C-Cu-MXene showed two main peaks at 1.5 and 2.2 Å, corresponding to the first Cu–O and the second Cu–Cu coordination shells, respectively [13]. The

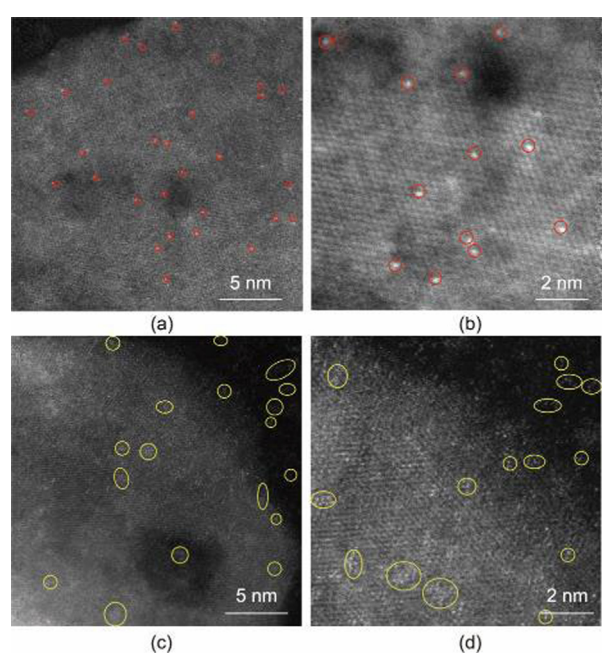

Fig. 1. The AC-HAADF-STEM images of (a) and (b) SA-Cu-MXene (Red circles); (c) and (d) C-Cu-MXene (Yellow circles).

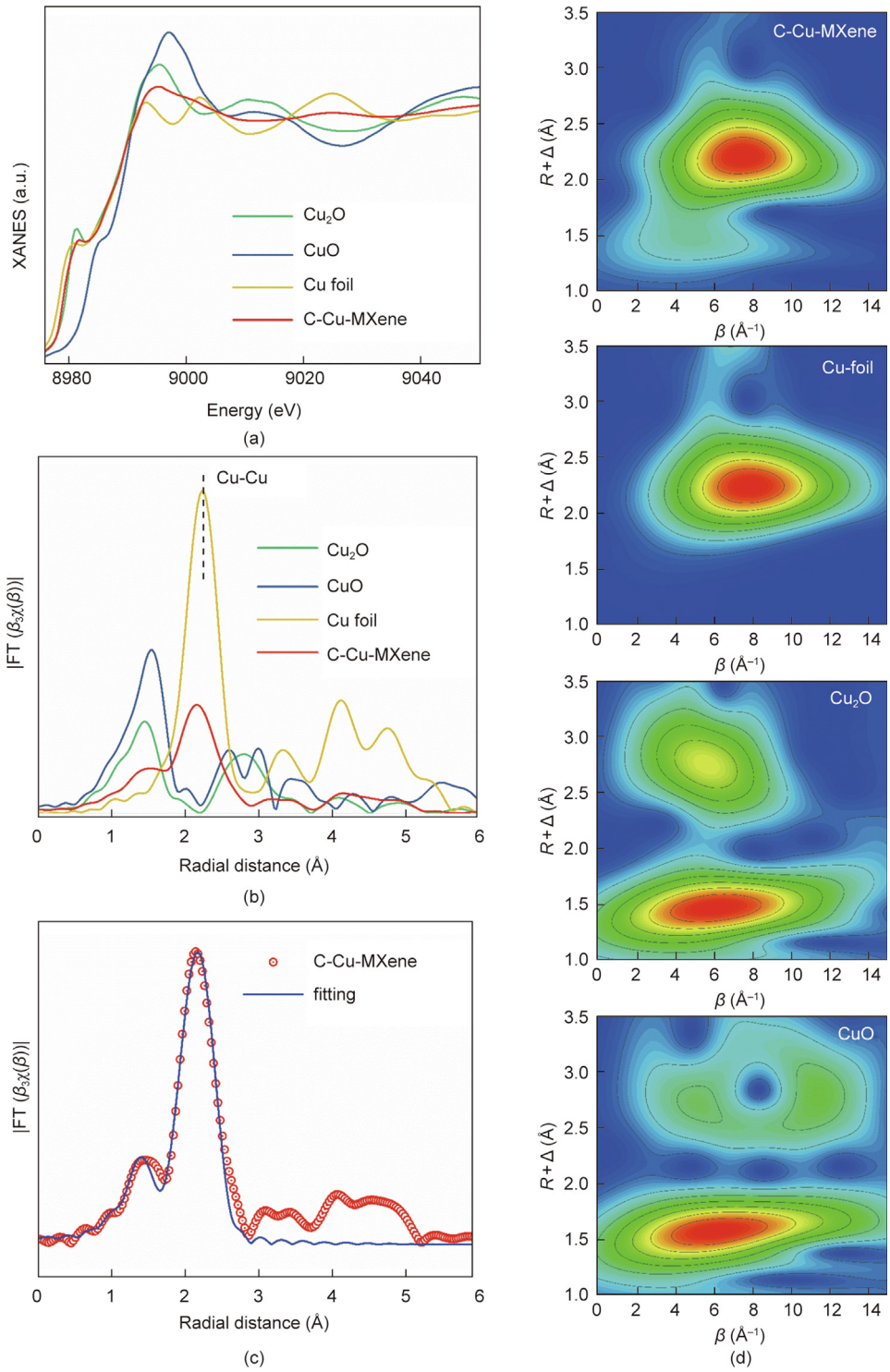

Fig. 2. (a) XANES spectra at the Cu K-edge with CuO, Cu_2O, and Cu foil as references; (b) The Fourier transform (FT) EXAFS spectra of the Cu foil, Cu_2O, CuO, and C-Cu-MXene samples; (c) EXAFS fitting curve of C-Cu-MXene; (d) WT plot of the Cu K-edge EXAFS for C-Cu-MXene sample and reference materials. *R*: the coordination bond length. *β*: the wave vector.

results indicated that Cu atoms were transformed into clusters and bonded to O atoms.

EXAFS fitting curves are shown in Fig. 2(c). In comparison with the wavelet transform (WT) plot of Cu_2O and CuO (Fig. 2(d)), the weak intensity of C-Cu-MXene was detected near 5.5–6 $Å^{-1}$, in accordance with the Cu–O path [31]. The WT contour plot of the C-Cu-MXene showed one intensity maximum at 7.5 $Å^{-1}$, associated with the Cu–Cu path in the second coordination shell [14]. These results provided further evidence for the formation of Cu clusters in the C-Cu-MXene catalyst. To further study the local structure and coordination environment of the Cu atoms in C-Cu-MXene, EXAFS was employed for further identification (Fig. 2(c)). According to the *R*-space fitting of the EXAFS parameters (Table S2 in Appendix A), the coordination number of the Cu 2nd

shell was approximately 5.20 and the average bond length of Cu was 2.52 Å. Cu_5 was regarded as the dominant Cu species. Furthermore, the coordination features of O 1st could be determined to be 1.21 in the C-Cu-MXene sample (Table S2).

3.2. Catalytic performance with different Cu distribution patterns

Fig. 3(a) showed the SMX degradation rate in Cu-decorated MXene/PMS systems. The SMX degradation rate was about 65.4% within 60 min in an SA-Cu-MXene system, which was 42.4% higher than that obtained in MXene/PMS system. Clearly, the single atom Cu played a significant role in PMS activation. Notably, the SMX degradation rate increased by 73.9% with the addition of C-Cu-MXene within 60 min compared with the control system. Obviously, C-Cu-MXene has affected the degradation of the contaminants in the PMS system considerably, which could be attributed to the high reactivity and selectivity of Cu clusters on the MXene surface. In comparison, the SMX degradation rate increased by only 16.2% after adding F-Cu-MXene, hence improving the PMS activation slightly. Additionally, the SMX degradation rate constants (k) were calculated as 0.0215, 0.0485, and 0.0082 min^{-1} for SA-Cu-MXene, C-Cu-MXene, and F-Cu-MXene based catalysts, respectively, in the PMS system.

Sequential experiments were carried out to investigate the reusability of the C-Cu-MXene catalyst. As illustrated in Fig. 3(b), the SMX degradation rate in C-Cu-MXene /PMS system was greater than 95% within 60 min after five cycles, exhibiting stable performance. Fig. 3(c) showed the PMS consumption in different catalytic systems. The PMS utilization rates were 58.0%, 76.8%, and 37.9% in the presence of SA-Cu-MXene, C-Cu-MXene, and F-Cu-MXene within 120 min, respectively. Moreover, the effective utilization rate of PMS in each system was calculated based on Text S2 in Appendix A. Effective utilization of PMS reached the optimum in the C-Cu-MXene system (about 61%), higher than those in the SA-Cu-MXene (48%) and F-Cu-MXene (21%). Obviously, the PMS activation efficiency was improved more evidently by the Cu cluster than single atom Cu and Cu film-loaded MXene. Worth mentioning, it was not straightforward to accurately control the Cu content and maintain consistency in the present experiments. Therefore, the quantitative relationship between the Cu content and the reaction constant was established. The Cu content of SA-Cu-MXene, C-Cu-MXene, and F-Cu-MXene catalysts were 0.15%, 0.26%, and 1.30%, respectively. As shown in Fig. 3(d), the k values under unit Cu content were normalized. Obviously, the k values per unit Cu content were 0.143 (single atom), 0.187 (clusters), and 0.006 min^{-1} (films), respectively. The above results indicated

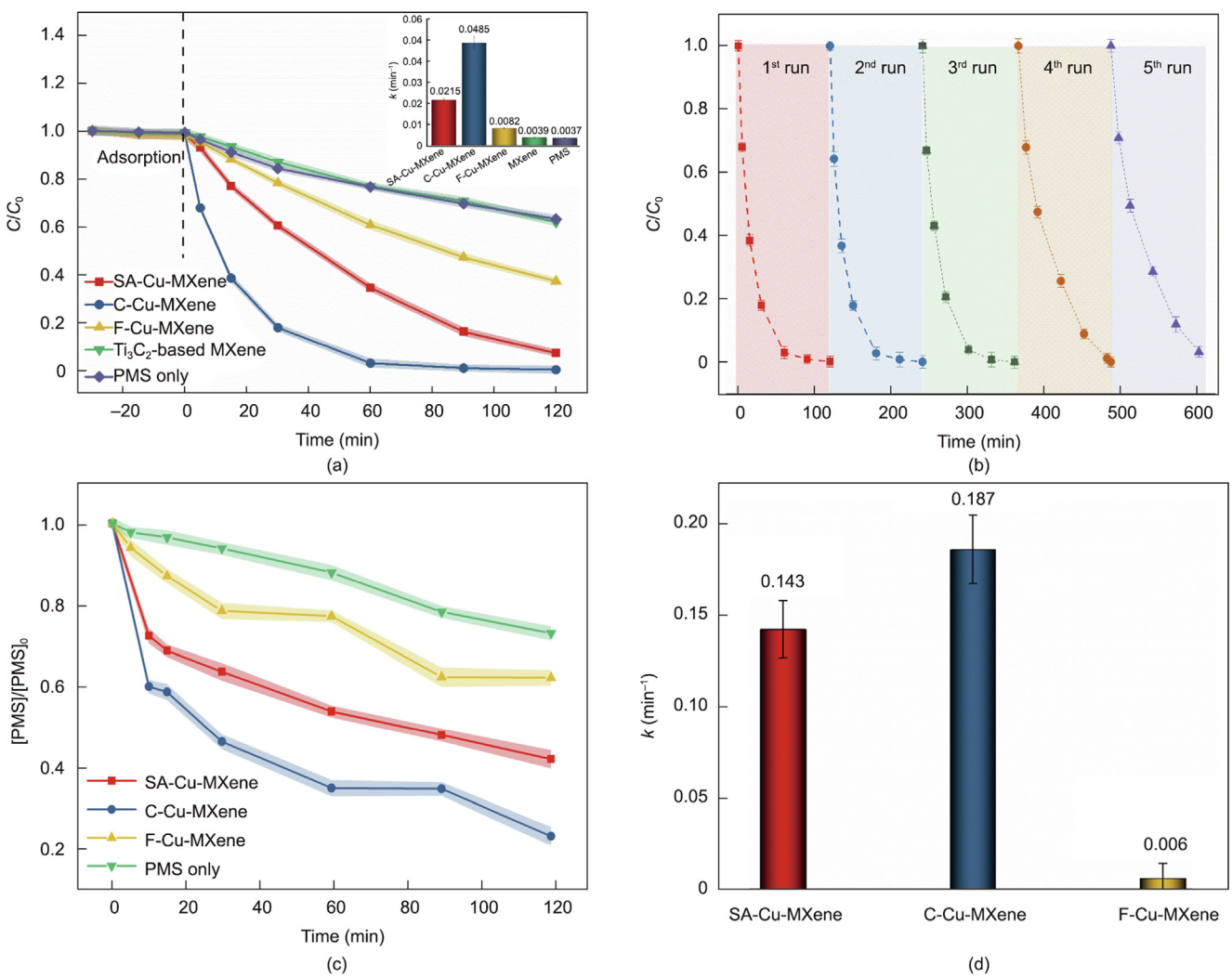

Fig. 3. (a) SMX concentration variation as a function of time with different catalysts in PMS system; (b) recycling test of C-Cu-MXene/PMS for SMX degradation; (c) utilization of PMS in different catalytic systems; (d) reaction rate constant normalized according to Cu content. Reaction conditions: T = 25 °C; pH = 7.4; the catalyst concentrations at 0 min (C_0(catalyst)) = 0.5 g·L^{-1}; C_0(PMS) = 1.2 mmol·L^{-1}; C_0(SMX) = 15 mg·L^{-1}.

that C-Cu-MXene possessed excellent performance for PMS activation and contaminants degradation.

The effect of solution pH (5.0, 7.4, and 9.0) on SMX removal efficiency was explored in C-Cu-MXene/PMS system (Fig. S7 in Appendix A). The C-Cu-MXene/PMS system in the neutral environments (pH 7.4) exhibited excellent performance for SMX degradation (>99%). Comparatively, the SMX removal rate was only 49.78% under acidic conditions (pH 5.0), which might contribute to the quenching of ·OH and $SO_4^{\bar{}}$· by H^+. Moreover, $SO_4^{\bar{}}$· reacted with OH^- under alkaline conditions, leading to the reduction of the oxidation capacity to SMX. The k values of SMX degradation were 0.0056, 0.0485, and 0.0064 min^{-1} in the C-Cu-MXene/PMS system at the solution pH of 5.0, 7.4, and 9.0, respectively. Therefore, superior performance was obtained under conditions of pH-neutral media.

3.3. Oxidation pathways with different Cu distribution patterns

EPR experiment was further conducted to detect $^1O_2$, ·OH, $SO_4^{\bar{}}$· and $O_2^{\bar{}}$· species. Generally, DMPO was used as a trapping agent for ·OH, $SO_4^{\bar{}}$·, and $O_2^{\bar{}}$·, while TEMP was applied for trapping of singlet oxygen ($^1O_2$). As shown in Fig. 4(a), a strong signal with an intensity ratio of 1:1:1 was observed for Cu-decorated MXene samples, demonstrating the generation of $^1O_2$ [32]. Besides, a signal with an intensity ratio of 1:2:2:1 was noticed (Fig. 4(b)), which was attributed to the DMPO-·OH adduct [33]. In addition, obvious signal peaks with intensities of 1:1:1:1 could be seen in the Cu-decorated MXene/PMS systems (Fig. 4(c)), which was identified as the DMPO-$O_2^{\bar{}}$· adduct.

Particularly, the unique intensity of TEMP-$^1O_2$, DMPO-·OH, and DMPO-$O_2^{\bar{}}$· increased gradually with time while the signal of DMPO-$SO_4^{\bar{}}$· (1:1:1:1:1:1:1) has only changed slightly, indicating the consistent generation of $^1O_2$, ·OH and $O_2^{\bar{}}$·. Thus, $^1O_2$, ·OH, $SO_4^{\bar{}}$·, and $O_2^{\bar{}}$· were formed in PMS catalytic systems, which might contribute to the SMX degradation.

Chemical probe experiments were conducted for qualitative and quantitative analysis of active species in different PMS catalytic systems. Typically, BA was used to detect the presence of ·OH and $SO_4^{\bar{}}$· ($k_{(\cdot OH,\ BA)}$ = 4.2 × 10^9 mol·L^{-1}·s^{-1} and $k_{(SO_4^{\bar{}},\ BA)}$ = 1.2 × 10^9 mol·L^{-1}·s^{-1}) [34,35]. NB could identify ·OH ($k_{(\cdot OH,\ NB)}$ = 4.7 × 10^9 mol·L^{-1}·s^{-1}) [5,35]. Besides, FFA was applied to measure $^1O_2$, ·OH, and $SO_4^{\bar{}}$· ($k_{(^1O_2,FFA)}$ = 1.2 × 10^8 mol·L^{-1}·s^{-1}, $k_{(\cdot OH,\ FFA)}$ = 1.5 × 10^{10} mol·L^{-1}·s^{-1}, and $k_{(SO_4^{\bar{}},\ FFA)}$ = 3.7 × 10^9 mol·L^{-1}·s^{-1}) [34–36]. As demonstrated in Fig. 4(d), FFA was degraded completely while only 65.8% of NB and 90.8% of BA were decomposed within 60 min in SA-Cu-MXene/PMS system. The reaction rate constants of NB, BA, and FFA were calculated and found to be 0.0185, 0.0340, and 0.2472 min^{-1}, respectively, revealing the major active species $^1O_2$ and $SO_4^{\bar{}}$·. As shown in Fig. 4(e), the degradation rate of BA and FFA reached up to nearly 100% and that of NB achieved only 68.2% within 20 min. Interestingly, the degradation rate constants of NB, BA, and FFA were 0.0203, 0.1240, and 0.4980 min^{-1}, respectively. The results reflected the poor contribution of ·OH in the C-Cu-MXene/PMS system. Comparatively, the reaction rate constants of BA, NB, and FFA were 0.0047, 0.0065, and 0.0339 min^{-1} in the F-Cu-MXene/PMS system, respectively (Fig. 4(f)). The results indicated the lowest PMS activation efficiency by the Cu film.

The steady-state concentration of $^1O_2$, $SO_4^{\bar{}}$·, and ·OH was calculated (Fig. 4(g)). Comparatively, the steady-state concentration of $SO_4^{\bar{}}$· was higher in C-Cu-MXene/PMS system. Particularly, the $^1O_2$ concentration reached the highest (4.7 × 10^{-10} mol·L^{-1}·s^{-1}) and was one and two orders of magnitude higher than $SO_4^{\bar{}}$· and ·OH concentrations (9.8 × 10^{-11} and 5.2 × 10^{-12} mol·L^{-1}·s^{-1}) in the C-Cu-MXene/PMS system. Obviously, large amounts of $^1O_2$ were generated in the SA-Cu-MXene/PMS and C-Cu-MXene/PMS system. Na_2CO_3 was selected to scavenge $O_2^{\bar{}}$· [37]. As shown in Fig. S8 in Appendix A, the SMX degradation rate remained almost unchanged in the presence of Na_2CO_3 in the three Cu-decorated MXene/PMS systems within 120 min. Apparently, $O_2^{\bar{}}$· also played a negligible role in the process of SMX degradation.

The relative contribution of $SO_4^{\bar{}}$·, ·OH, and $^1O_2$ to SMX degradation was then estimated using Eqs. (S9)–(S11) in Appendix A. The obtained results are shown in Fig. 4(h). The second-order rate constants for the reaction of SMX with $SO_4^{\bar{}}$·, ·OH, and $^1O_2$ were presented in Appendix A Table S4. In general, $^1O_2$ played an insignificant role in the abatement of contaminants (contribution ≈ 0). Notably, $SO_4^{\bar{}}$· played a dominant role in the SA-Cu-MXene and C-Cu-MXene activated PMS systems (contribution > 90%). The contribution of ·OH was negligible in the SA-Cu-MXene and C-Cu-MXene activated PMS systems. Consistently, $SO_4^{\bar{}}$· and ·OH contributed 71.9% and 28.1% to SMX degradation in the F-Cu-MXene/PMS system. Obviously, a large amount of $^1O_2$ was produced in the C-Cu-MXene/PMS system, but it did not play a significant role in contaminant degradation. However, pollutants were degraded through the $SO_4^{\bar{}}$· oxidation with strong ability.

In summary, radical pathways (i.e., $SO_4^{\bar{}}$· and ·OH) played major roles in SMX degradation in the SA-Cu-MXene, C-Cu-MXene, and F-Cu-MXene/PMS systems. The steady-state concentrations of $^1O_2$ were 3.9 × 10^{-10}, 1.6 × 10^{-9}, and 8.8 × 10^{-11} mol·L^{-1}·s^{-1}, which is higher than those of $SO_4^{\bar{}}$· and ·OH in the corresponding three Cu-decorated MXene systems. The contribution of $SO_4^{\bar{}}$· oxidation to SMX degradation was 90.4%, 97.3%, and 71.9% with the Cu distribution pattern changed from single atom to films. It is worth noting that $SO_4^{\bar{}}$· with high redox potential contributed to a higher reaction rate of SMX in the C-Cu-MXene/PMS system. On the contrary, the $^1O_2$ oxidation routes contributed negligibly to SMX degradation in the three Cu-decorated MXene/PMS systems.

3.4. Evaluation of bond length, adsorption energy, and electron density

The optimization configurations of SA-Cu-MXene, C-Cu-MXene, and F-Cu-MXene samples were shown in Figs. 5(a)–(c). DFT theory calculation predicted changes in the bond length of O—O (l_{O-O}) and adsorption energy (E_{ads}) of PMS molecules with stable adsorption of PMS on the Cu-decorated MXene. The E_{ads} of PMS on the SA-Cu-MXene, C-Cu-MXene, and F-Cu-MXene surfaces were −4.236, −5.435, and −3.548 eV, respectively. Therefore, PMS tends to prefer to adsorb on the C-Cu-MXene surface for activation. Clearly, the l_{O-O} value of PMS adsorption on C-Cu-MXene (l_{O-O} = 1.476 Å) was higher than those obtained on SA-Cu-MXene (l_{O-O} = 1.469 Å) and F-Cu-MXene (l_{O-O} = 1.462 Å). In comparison with the O–O bond length of PMS molecules (l_{O-O} = 1.332 Å) in a vacuum, the extended O–O bond of PMS adsorbed on the C-Cu-MXene indicated that the PMS molecules could be better activated. Subsequently, the cleavage of the O–O bond in PMS was ready to produce ROS.

The electron density distribution between PMS and Cu-decorated MXene was further explored by electron density difference (EDD) analysis. EDD was defined as:

$$\Delta\rho(r) = \rho_{system}(r) - \rho_{surface}(r) - \rho_{HSO_5^-}(r) \quad (2)$$

where $\rho_{system}(r)$, $\rho_{surface}(r)$, and $\rho_{HSO_5^-}(r)$ are the electronic densities of Cu-decorated MXene/PMS, Cu-decorated MXene, and PMS, respectively.

The charge density difference and the number of electron transfers between different Cu-decorated MXene models and PMS were presented in Figs. 5(d)–(e). A strong redistribution of electron density could be observed between the Cu atoms of Cu-decorated MXene models and the O atoms of HSO_5^- (Cu → O). Based on the electron transfer calculated by Bader [17], the electron transfer (Q) between Cu-decorated MXene and PMS could be obtained ($Q_{SA\text{-}Cu\text{-}MXene}$ = 0.923 e, $Q_{C\text{-}Cu\text{-}MXene}$ = 1.056 e, and $Q_{F\text{-}Cu\text{-}MXene}$ = 0.847 e).

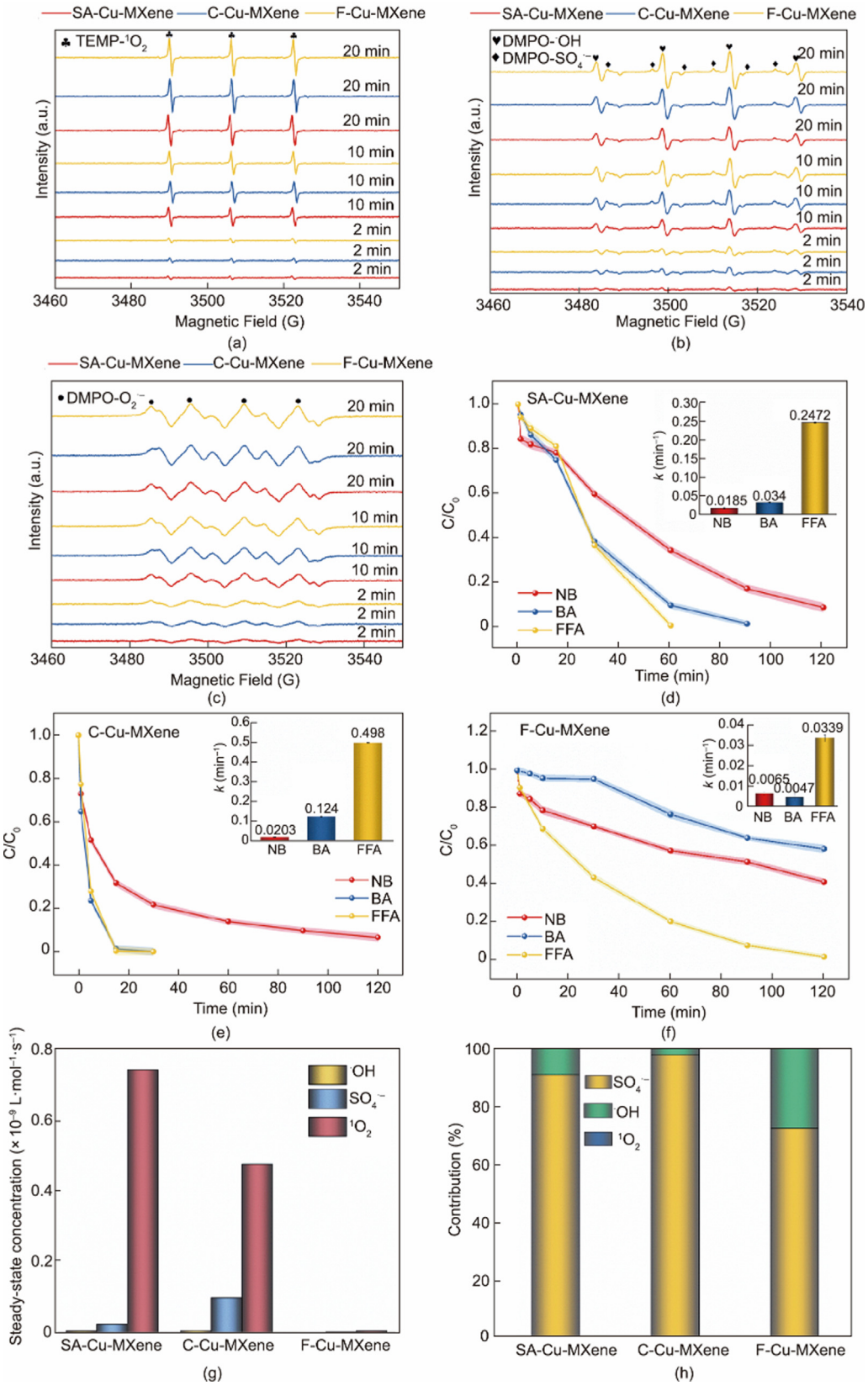

Fig. 4. EPR spectra of (a) $^1O_2$ in the presence of TEMP, (b) $\cdot OH/SO_4^{\cdot-}$ in the presence of DMPO, (c) $O_2^{\cdot-}$ in the presence of DMPO, degradation of NB, BA, and FFA in the Cu-based catalytic PMS systems: (d) SA-Cu-MXene, (e) C-Cu-MXene, and (f) F-Cu-MXene with corresponding kinetic rate constants inserted; (g) steady-state concentration of active species; (h) contribution of oxidative species to SMX degradation. Reaction conditions: T = 25 °C; pH = 7.4 C_0(catalyst) = 0.5 g·L^{-1}; C_0(PMS) = 1.2 mmol·L^{-1}; C_0(SMX) = 15 mg·L^{-1}. a.u.: arbitrary unit.

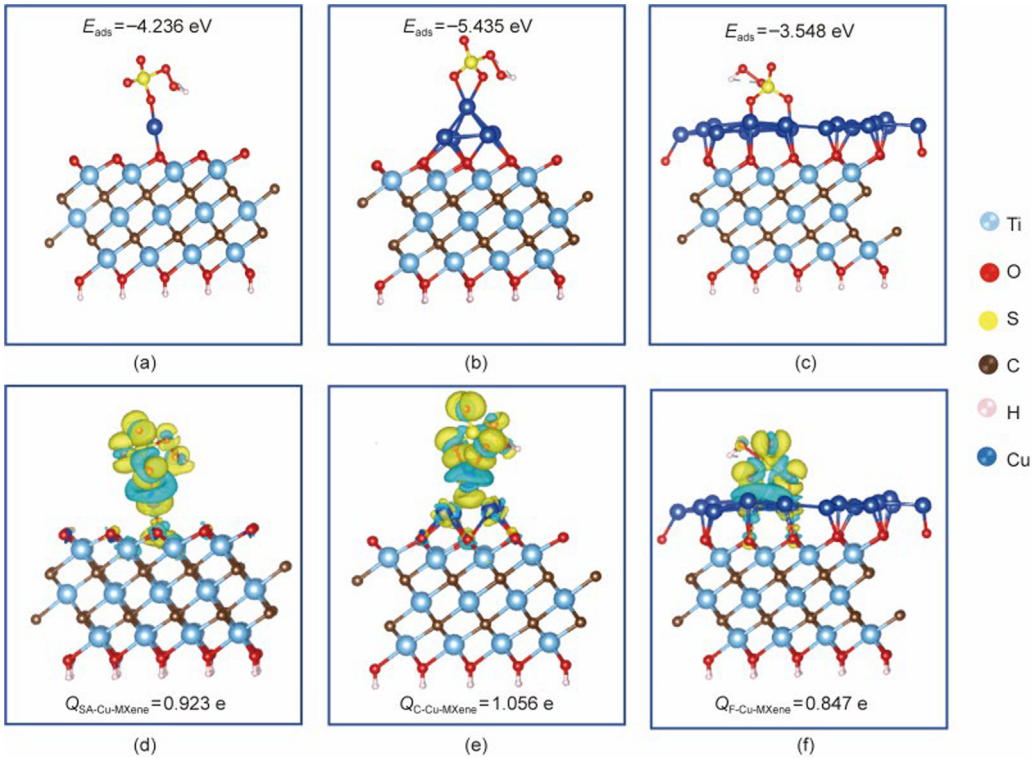

Fig. 5. Optimization configurations of (a) SA-Cu-MXene, (b) C-Cu-MXene, and (c) F-Cu-MXene and electron density difference and the number of electron transfer between (d) SA-Cu-MXene, (e) C-Cu-MXene, (f) F-Cu-MXene, and PMS (the yellow and cyan colors represent the electron accumulation and deletion, respectively).

Obviously, the interaction between HSO_5^- and Cu atoms in C-Cu-MXene was stronger, demonstrating that PMS is prone to adsorb at the Cu position of C-Cu-MXene. No obvious electron density redistribution was observed between the Cu and O atoms on the MXene substrate. Hence, the C-Cu-MXene promoted PMS activation, in which the loaded Cu cluster was the main active site.

Activation pathways of PMS on SA-Cu-MXene, C-Cu-MXene, and F-Cu-MXene surfaces as well as adsorption energy between catalysts and PMS at different stages were illustrated in Fig. 6. The reaction energy of PMS absorbed on the C-Cu-MXene (ΔE = − 6.435 eV) was more negative than those of SA-Cu-MXene (ΔE = − 4.236 eV), and F-Cu-MXene (ΔE = − 3.548 eV). From the view of thermodynamic feasibility, the present findings confirm that C-Cu-Mxene was more inclined to the first reaction step.

The adsorption energy values of SA-Cu-MXene (ΔE = − 4.539 eV) and F-Cu-MXene (ΔE = − 4.067 eV) were more negative than that of C-Cu-MXene (ΔE = − 3.878 eV) sample in step 3, demonstrating that PMS in C-Cu-MXene/PMS system had more difficulty in adsorption. However, it was easier for $SO_4^{\cdot-}$ to desorb from the C-Cu-MXene/PMS system, resulting in higher concentration than SA-Cu-MXene and F-Cu-MXene activated PMS systems. Noticeably, only partial catalyst-OH could react with PMS, generating catalyst-$^1O_2$. The remaining catalyst-OH desorbed and produced ·OH. Conversely, the adsorption energy in step 5 in C-Cu-MXene/PMS was the most negative ($\Delta E_{SA\text{-}Cu\text{-}MXene}$ = − 3.165 eV, $\Delta E_{C\text{-}Cu\text{-}MXene}$ = − 3.576 eV, and $\Delta E_{F\text{-}Cu\text{-}MXene}$ = − 2.051 eV), which is an indication that the generated $^1O_2$ at the catalyst sites was the most likely to desorb. Overall, the concentration of oxidative species in the C-Cu-MXene/PMS system was the highest.

3.5. Degradation routes and toxicity changes with different Cu distribution patterns

As shown in Appendix A Fig. S9, the removal efficiencies of TOC were 48.2%, 55.6%, and 34.5% within 120 min in SA-Cu-MXene, C-Cu-MXene and F-Cu-MXene activated PMS systems, respectively. Clearly, the higher mineralization rate of SMX was obtained in the C-Cu-MXene/PMS system, which might be attributed to the larger contribution of $SO_4^{\cdot-}$. The possible degradation routes of SMX were proposed based on LC–MS analysis. As depicted in Fig. 7, some intermediates such as P1–P3, P5, and P8–P16 appeared during SMX degradation. Notably, more special intermediates including P4, P6, P7, and P8 were generated in the C-Cu-MXene/PMS system. The pathway of SMX degradation might be more complex with C-Cu-MXene activation compared to SA-Cu-MXene and F-Cu-MXene activation. As presented in Fig. 4(h), $SO_4^{\cdot-}$ played a dominant role in SMX degradation. According to previous reports, the sulfonamide bond (S—N bond), methyl (—CH_3) group in isoxazole, and an amine group (—NH_2) in the benzene ring might be the preferred sites to be attacked in SMX [38,39]. Four pathways of SMX degradation in the Cu-decorated MXene/PMS systems were proposed (Fig. 7). For P1, the S–N bond in SMX was attacked by oxidative species and cleaved, forming P1 and P2. Note that little P2 was detected in the C-Cu-MXene/PMS system, being attributed to the ring-opening conversion of partial P2 to less toxic P4. The higher contribution of $SO_4^{\cdot-}$ oxidative species in the C-Cu-MXene/PMS system possessed strong oxidative ability, hence promoting the opening of the isoxazole ring.

In addition, the benzene ring in SMX was prone to hydroxylate (pathways 1 and 2). During this hydroxylation, the solubility of pollutants could be improved, which can be beneficial for SMX degradation. Obviously, SMX and corresponding degradation intermediates were more likely to be hydroxylated in the C-Cu-MXene/PMS system. For instance, the signals of P6 and P7 could only be detected in the C-Cu-MXene/PMS system, which might be ascribed to the simultaneous appearance of $SO_4^{\cdot-}$ and ·OH. The $SO_4^{\cdot-}$ reacted with electron-rich organic moieties (e.g., aniline) through single-electron transfer and then produced radical cations [36]. Radical cations reacted with water rapidly through hydroxyl extraction or addition reactions, forming hydroxylated intermediates.

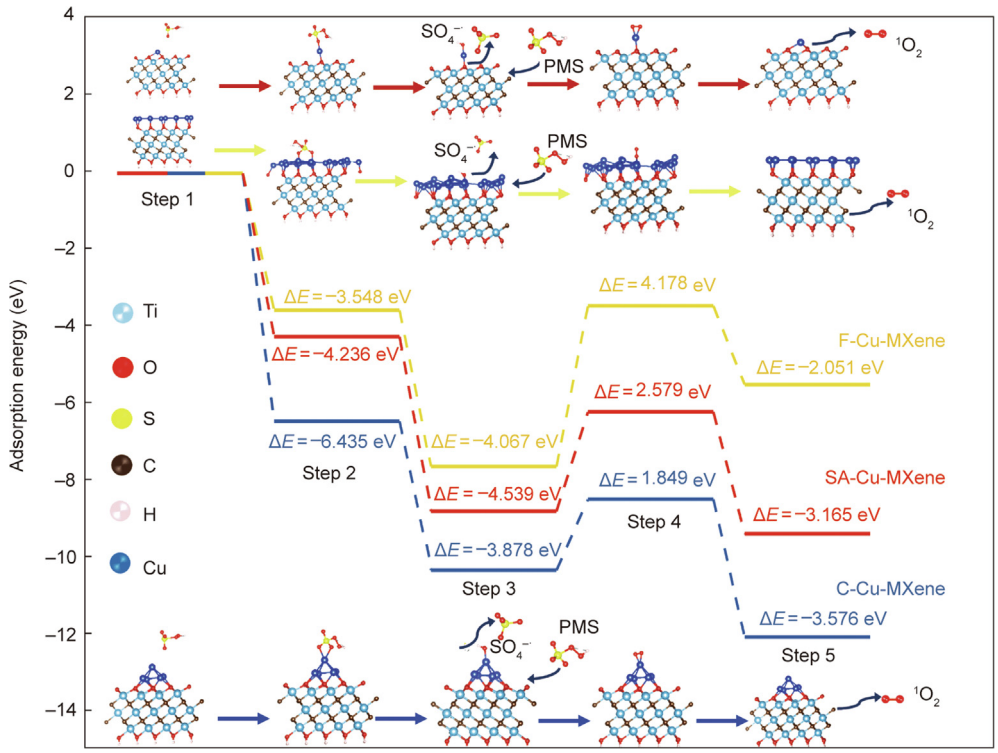

Fig. 6. Proposed mechanism of oxidative species production via PMS activation with different catalysts.

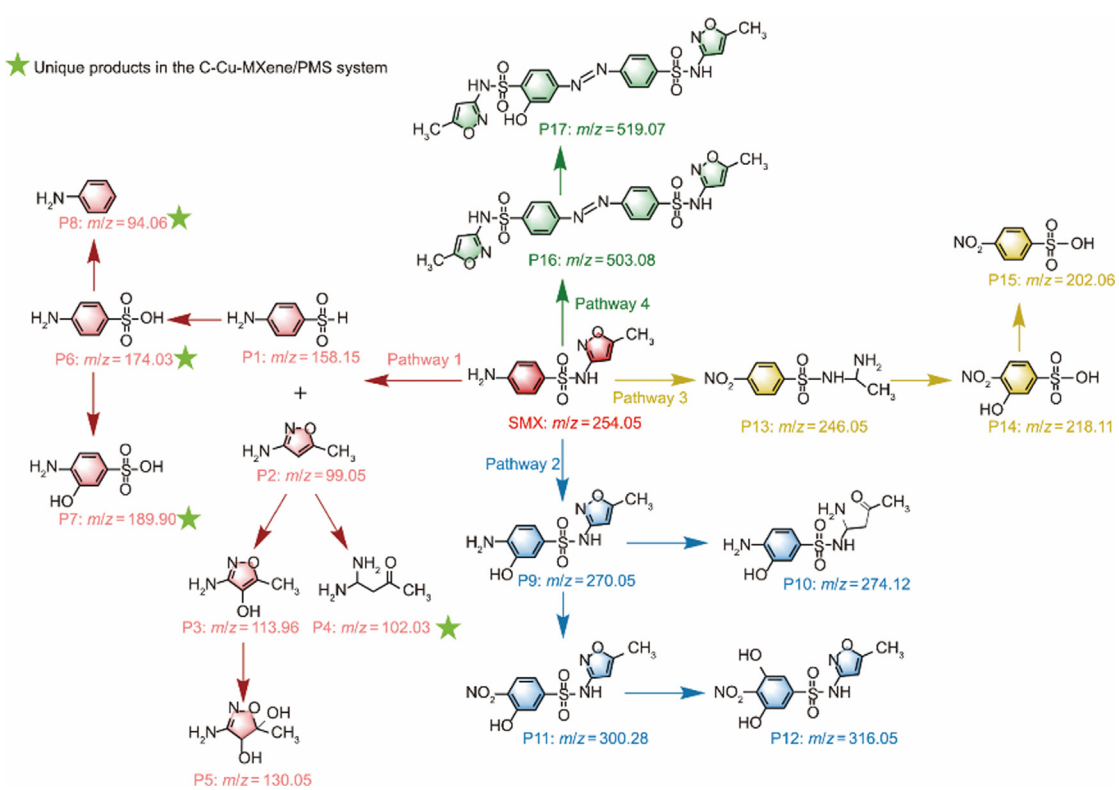

Fig. 7. Possible pathways of SMX degradation by Cu-decorated MXene/PMS systems. m/z: mass-to-charge ratio.

Remarkably, the mono hydroxylation was prone to occur at the ortho-position of $-NH_2$ in the benzene ring of SMX (P7, P9, and P11). This phenomenon could be attributed to the electron-donating effect of $-NH_2$ and the electron-withdrawing effect of $-SO_2-NH$ [36]. Furthermore, the hydroxyl group could increase the electron density of contaminants, activating aromatic rings.

Therefore, monohydroxylated products could be further attacked by electrophilic species, generating polyhydroxylated compounds (e.g., P12).

In pathway 3, reactive species (mainly $SO_4^{-}\cdot$ and $\cdot OH$) attacked SMX, resulting in the oxidation of the amine group in the benzene ring and the cleavage of the C–C bond in the isoxazole ring. Then, P13 was formed, which was further converted to P14 through the cleavage of the C–N bond. P16 and P17 could be detected in the three Cu-decorated MXene/PMS systems, being ascribed to the amino-coupling of SMX molecules (pathway 4). Subsequently, P16 was further hydroxylated to P17. In comparison with SA-Cu-MXene and F-Cu-MXene activated PMS systems, the C-Cu-MXene/PMS system produced fewer intermediates with high m/z value. Obviously, the C-Cu-MXene/PMS system exhibited a higher degradation degree towards SMX with the co-existence of both $SO_4^{-}\cdot$ and $\cdot OH$. Specifically, $SO_4^{-}\cdot$ might attack the sulfonyl group. Therefore, it was difficult to form coupling products in the C-Cu-MXene system, and products with lower m/z values were generated relatively.

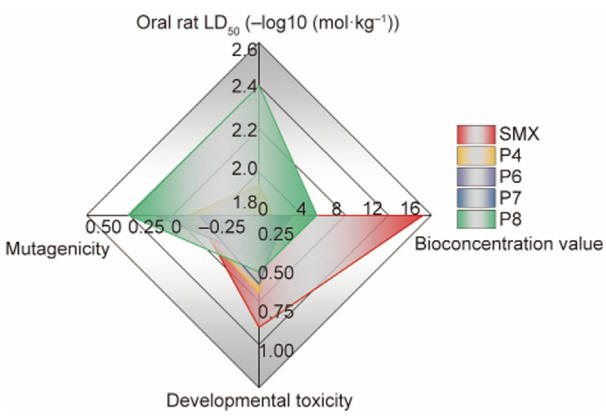

Fig. 8. Theoretical calculated developmental toxicity, bioconcentration factor, mutagenicity, and oral rat LD_{50} of SMX and typical degradation intermediates in C-Cu-MXene/PMS system.

To investigate the toxicity changes during SMX degradation in different Cu-decorated MXene/PMS systems, the toxicity estimation software tool based on quantitative structure–activity relationship models was applied [40,41]. The developmental toxicity, bioconcentration factor, mutagenicity, and oral lethal dose (LD_{50}) values of SMX and typical oxidation intermediates in the C-Cu-MXene/PMS were presented in Fig. 8. The toxicity changes of the remaining intermediates in the three Cu-decorated MXene/PMS systems were shown in Appendix A Fig. S10. SMX with developmental toxicity value of 0.85 was considered as "developmental toxicant ($\geq$ 0.5)". Most intermediates exhibited similar or lower developmental toxicity values compared to SMX. Furthermore, the four products only formed in the C-Cu-MXene/PMS system exhibited relatively low developmental toxicity values, of which P6 showed no developmental toxicity. Therefore, a greater reduction in developmental toxicity could be achieved after SMX degradation in the C-Cu-MXene/PMS system, which was superior to the SA-Cu-MXene and F-Cu-MXene/PMS systems. In addition, the bioconcentration factors of all intermediates dropped compared to those of SMX (Fig. S10(b)). The "mutagenicity negative (< 0.5)" of SMX and its degradation intermediates were illustrated in Fig. S10(c), revealing non-mutagenic properties. The oral rat LD_{50} index represented the number of chemicals that caused the death of half of the rats after oral ingestion. The LD_{50} value of most intermediates increased sharply, while only that of P7 decreased slightly, implying a weakness in acute toxicity after SMX degradation (Fig. S10(d)). Generally, SMX degradation in the three Cu-decorated MXene/PMS systems could be speculated as green processes with less toxicity. Obviously, the C-Cu-MXene/PMS system showed more advantages. However, a few toxic intermediates still existed after SMX degradation. The catalytic oxidation systems need to be further optimized.

Based on the above results, SMX degradation mechanisms with different Cu distribution patterns were proposed in the PMS systems (Fig. 9). The radical route played a dominant role in the three Cu-decorated MXene/PMS systems. $SO_4^{-}\cdot$ attacked the aniline ring

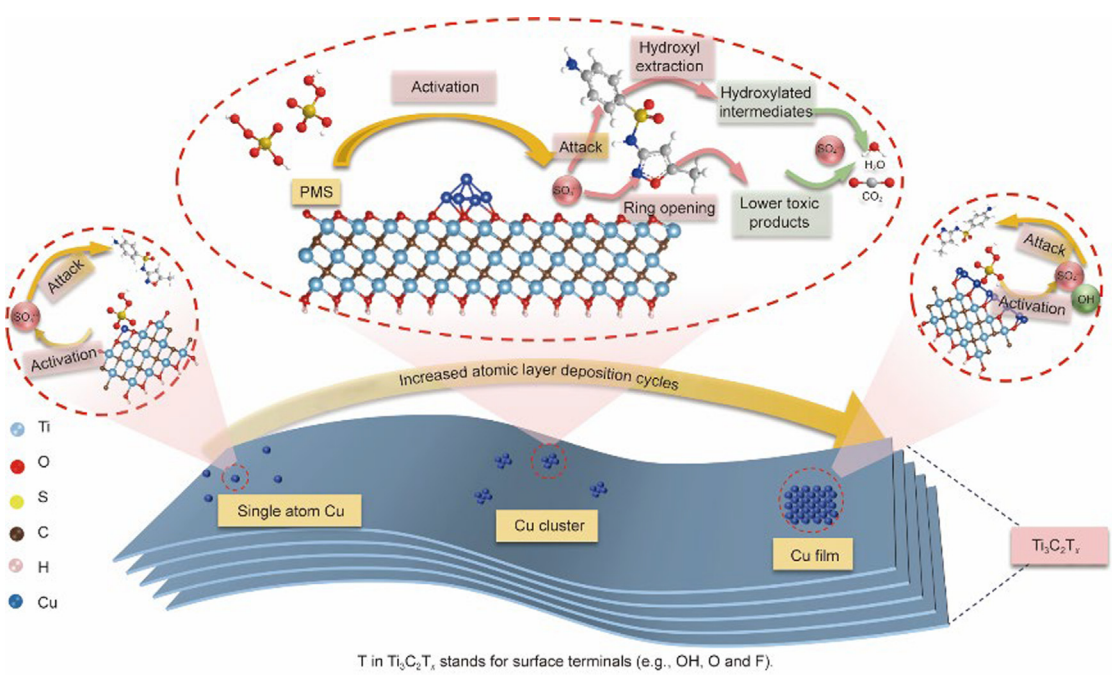

Fig. 9. Schematic diagram of SMX degradation in the Cu-decorated MXene/PMS systems.

in SMX, resulting in the ring opening. Moreover, $SO_4^{\cdot-}$ could react with the electron-rich moiety of SMX. Subsequently, hydroxylated intermediates were generated through hydroxyl group extraction or addition reactions between radical cations and water molecules, increasing the electron density of SMX. Therefore, the aromatic rings were activated. $SO_4^{\cdot-}$ with strong oxidation ability attacked the isoxazole ring of SMX, which is beneficial for the formation of less toxic products. Briefly, the C-Cu-MXene/PMS system demonstrated great application potential in the field of water treatment.

4. Conclusion

In this work, the metal distribution patterns of heterogeneous catalysts were modified by controlling the ALD cycle number, improving metal site utilization, and altering the reaction mechanism. In detail, the SMX degradation efficiency in C-Cu-MXene/PMS system was higher than that in SA-Cu-MXene and F-Cu-MXene activated PMS systems. Generally, Cu distribution patterns altered the types and concentrations of oxidative species, resulting in changes in oxidative species' contribution to SMX degradation. The contribution of $SO_4^{\cdot-}$ oxidation to SMX degradation was 90.4%, 97.3%, and 71.9% with the Cu distribution pattern changed from single atom to films. Obviously, the three Cu-decorated MXene/PMS systems exhibited different oxidation capacities for contaminant degradation. Four different SMX degradation pathways were proposed in Cu-decorated MXene/PMS systems. Specifically, four lower toxic intermediates were produced solely in the C-Cu-MXene/PMS system. Both experimental investigations and DFT calculations showed that the Cu cluster represented the active sites on the C-Cu-MXene surface, which could adsorb PMS effectively (E_{ads} = − 5.435 eV) and prolong the O—O bond of PMS (from 1.332 Å in vacuum to 1.476 Å in adsorption). Explicitly, we followed a novel strategy for designing heterogeneous catalysts, and our findings revealed changes in the catalytic oxidation mechanisms induced by metal distribution patterns. Hence, catalysts with different metal distribution configurations could be selected according to the treatment demand of actual water. Subsequently, the active species composition of a catalytic PMS system could be controlled to improve oxidative selectivity. Furthermore, it was conducive to make full use of ROS, saving metal-based catalysts and the amount of the oxidant.

Declaration of competing interest

The authors declare that they have no known competing financial interests or personal relationships that could have appeared to influence the work reported in this paper.

Acknowledgments

The authors would like to express gratitude to the National Natural Science Foundation of China (52100156), the Natural Science Foundation of Tianjin (21JCQNJC00400), and the Shenzhen Science and Technology Program (GJHZ20200731095801005 and JCYJ20200109150210400) for financial support to this research.

Appendix A. Supplementary material

Supplementary data to this article can be found online at https://doi.org/10.1016/j.eng.2023.07.020.

References

[1] Mi X, Zhong H, Zhang H, Xu S, Li Y, Wang H, et al. Facilitating redox cycles of copper species by pollutants in peroxymonosulfate activation. Environ Sci Technol 2022;56(4):2637–46.
[2] Lee J, von Gunten U, Kim JH. Persulfate-based advanced oxidation: critical assessment of opportunities and roadblocks. Environ Sci Technol 2020;54(6):3064–81.
[3] Zeng T, Zhang X, Wang S, Niu H, Cai Y. Spatial confinement of a Co_3O_4 catalyst in hollow metal-organic frameworks as a nanoreactor for improved degradation of organic pollutants. Environ Sci Technol 2015;49(4):2350–7.
[4] Meng C, Ding B, Zhang S, Cui L, Ostrikov KK, Huang Z, et al. Angstrom-confined catalytic water purification within Co-TiO_x laminar membrane nanochannels. Nat Commun 2022;13(1):4010.
[5] Huang B, Xiong Z, Zhou P, Zhang H, Pan Z, Yao G, et al. Ultrafast degradation of contaminants in a trace cobalt(II) activated peroxymonosulfate process triggered through borate: indispensable role of intermediate complex. J Hazard Mater 2022;424(Pt D):127641.
[6] Guo D, Liu Y, Ji H, Wang CC, Chen B, Shen C, et al. Silicate-enhanced heterogeneous flow-through electro-fenton system using iron oxides under nanoconfinement. Environ Sci Technol 2021;55(6):4045–53.
[7] Cai P, Zhao J, Zhang X, Zhang T, Yin G, Chen S, et al. Synergy between cobalt and nickel on $NiCo_2O_4$ nanosheets promotes peroxymonosulfate activation for efficient norfloxacin degradation. Appl Catal B 2022;306:121091.
[8] Chen YD, Wang R, Duan X, Wang S, Ren NQ, Ho SH. Production, properties, and catalytic applications of sludge derived biochar for environmental remediation. Water Res 2020;187:116390.
[9] Gao Y, Zhu Y, Lyu L, Zeng Q, Xing X, Hu C. Electronic structure modulation of graphitic carbon nitride by oxygen doping for enhanced catalytic degradation of organic pollutants through peroxymonosulfate activation. Environ Sci Technol 2018;52(24):14371–80.
[10] Tam Do M, Ncibi MC, Srivastava V, Thangaraj SK, Janis J, Sillanpaa M. Gingerbread ingredient-derived carbons-assembled CNT foam for the efficient peroxymonosulfate-mediated degradation of emerging pharmaceutical contaminants. Appl Catal B 2019;244:367–84.
[11] Wang Y, Song Y, Li N, Liu W, Yan B, Yu Y, et al. Tunable active sites on biogas digestate derived biochar for sulfanilamide degradation by peroxymonosulfate activation. J Hazard Mater 2022;421:126794.
[12] Jin L, You S, Ren N, Ding B, Liu Y. Mo vacancy-mediated activation of peroxymonosulfate for ultrafast micropollutant removal using an electrified MXene filter functionalized with Fe single atoms. Environ Sci Technol 2022;56(16):11750–9.
[13] Li F, Lu Z, Li T, Zhang P, Hu C. Origin of the excellent activity and selectivity of a single-atom copper catalyst with unsaturated Cu-N_2 sites via peroxydisulfate activation: Cu(III) as a dominant oxidizing species. Environ Sci Technol 2022;56(12):8765–75.
[14] Liu J, He H, Shen Z, Wang HH, Li W. Photoassisted highly efficient activation of persulfate over a single-atom Cu catalyst for tetracycline degradation: process and mechanism. J Hazard Mater 2022;429:128398.
[15] Yao C, Guo N, Xi S, Xu CQ, Liu W, Zhao X, et al. Atomically-precise dopant-controlled single cluster catalysis for electrochemical nitrogen reduction. Nat Commun 2020;11(1):4389.
[16] Hu Q, Gao K, Wang X, Zheng H, Cao J, Mi L, et al. Subnanometric Ru clusters with upshifted D band center improve performance for alkaline hydrogen evolution reaction. Nat Commun 2022;13(1):3958.
[17] Peng L, Duan X, Shang Y, Gao B, Xu X. Engineered carbon supported single iron atom sites and iron clusters from Fe-rich *Enteromorpha* for Fenton-like reactions via nonradical pathways. Appl Catal B Environ 2021;287:119963.
[18] Wang X, Xiong Z, Shi H, Wu Z, Huang B, Zhang H, et al. Switching the reaction mechanisms and pollutant degradation routes through active center size-dependent Fenton-like catalysis. Appl Catal B Environ 2023;329:122569.
[19] Fonseca J, Lu J. Single-atom catalysts designed and prepared by the atomic layer deposition technique. ACS Catal 2021;11(12):7018–59.
[20] Nimai S, Zhang H, Wu Z, Li N, Lai B. Efficient degradation of sulfamethoxazole by acetylene black activated peroxydisulfate. Chinese Chem Lett 2020;31(10):2657–60.
[21] Wang Y, Zhou C, Wu J, Niu J. Insights into the electrochemical degradation of sulfamethoxazole and its metabolite by Ti/SnO_2-Sb/Er-PbO_2 anode. Chinese Chem Lett 2020;31(10):2673–7.
[22] Wang Y, Peng W, Wang J, Chen G, Li N, Song Y, et al. Sulfamethoxazole degradation by regulating active sites on distilled spirits lees-derived biochar in a continuous flow fixed bed peroxymonosulfate reactor. Appl Catal B 2022;310:121342.
[23] Kresse G. Ab initio molecular dynamics for liquid metals. J Non-Cryst Solids 1995;192–193:222–9.
[24] Kresse G, Furthmüller J. Efficient iterative schemes for ab initio total-energy calculations using a plane–wave basis set. Phys Rev B Condens Matter 1996;54(16):11169–86.
[25] Kresse G, Furthmüller J. Efficiency of ab-initio total energy calculations for metals and semiconductors using a plane–wave basis set. Comput Mater Sci 1996;6(1):15–50.
[26] Kresse G, Hafner J. Ab initio molecular-dynamics simulation of the liquid-metal-amorphous-semiconductor transition in germanium. Phys Rev B Condens Matter 1994;49(20):14251–69.

[27] Kresse G, Joubert D. From ultrasoft pseudopotentials to the projector augmented-wave method. Phys Rev B Condens Matter Mater Phys 1999;59(3):1758–75.
[28] Perdew JP, Burke K, Ernzerhof M. Generalized gradient approximation made simple. Phys Rev Lett 1996;77(18):3865–8.
[29] Grimme S, Antony J, Ehrlich S, Krieg H. A consistent and accurate ab initio parametrization of density functional dispersion correction (DFT-D) for the 94 elements H-Pu. J Chem Phys 2010;132(15):154104.
[30] Chadi DJ. Special points for Brillouin-zone integrations. Phys Rev B 1977;16(4):1746–7.
[31] Bao H, Qiu Y, Peng X, Wang JA, Mi Y, Zhao S, et al. Isolated copper single sites for high-performance electroreduction of carbon monoxide to multicarbon products. Nat Commun 2021;12(1):238.
[32] Zhou X, Luo C, Luo M, Wang Q, Wang J, Liao Z, et al. Understanding the synergetic effect from foreign metals in bimetallic oxides for PMS activation: a common strategy to increase the stoichiometric efficiency of oxidants. Chem Eng J 2020;381:122587.
[33] Gao Y, Chen Z, Zhu Y, Li T, Hu C. New insights into the generation of singlet oxygen in the metal-free peroxymonosulfate activation process: important role of electron-deficient carbon atoms. Environ Sci Technol 2020;54(2):1232–41.
[34] Dong H, Li Y, Wang S, Liu W, Zhou G, Xie Y, et al. Both Fe(IV) and radicals are active oxidants in the Fe(II)/peroxydisulfate process. Environ Sci Technol Lett 2020;7(3):219–24.
[35] Zhu S, Li X, Kang J, Duan X, Wang S. Persulfate activation on crystallographic manganese oxides: mechanism of singlet oxygen evolution for nonradical selective degradation of aqueous contaminants. Environ Sci Technol 2019;53(1):307–15.
[36] He D, Yang H, Jin D, Qu J, Yuan X, Zhang YN, et al. Rapid water purification using modified graphitic carbon nitride and visible light. Appl Catal B 2021;285:119864.
[37] Cheng X, Guo H, Zhang Y, Wu X, Liu Y. Non-photochemical production of singlet oxygen via activation of persulfate by carbon nanotubes. Water Res 2017;113:80–8.
[38] Hu J, Li X, Liu F, Fu W, Lin L, Li B. Comparison of chemical and biological degradation of sulfonamides: solving the mystery of sulfonamide transformation. J Hazard Mater 2022;424(Pt D):127661.
[39] Wang A, Ni J, Wang W, Wang X, Liu D, Zhu Q. MOF-derived N-doped ZnO carbon skeleton@hierarchical Bi_2MoO_6 S-scheme heterojunction for photodegradation of SMX: mechanism, pathways and DFT calculation. J Hazard Mater 2022;426:128106.
[40] Cai Z, Hao X, Sun X, Du P, Liu W, Fu J. Highly active WO_3@anatase-SiO_2 aerogel for solar-light-driven phenanthrene degradation: mechanism insight and toxicity assessment. Water Res 2019;162:369–82.
[41] Liang L, Wang Y, Li N, Yan B, Chen G, Hou LA. Breaking rate-limiting steps in a red mud-sewage sludge carbon catalyst activated peroxymonosulfate system: effect of pyrolysis temperature. Separ Purif Tech 2022;299:121805.